ELSEVIER

Volume 183, Issue 7, July 2010

JOURNAL OF SOLID STATE CHEMISTRY

www.elsevier.com/locate/jssc

CONTENTS

Abstracted/indexed in BioEngineering Abstracts, Chemical Abstracts, Coal Abstracts, Current Contents/Physics, Chemical, & Earth Sciences, Engineering Index, Research Alert, SCISEARCH, Science Abstracts, and Science Citation Index. Also covered in the abstract and citation database SCOPUS®. Full text available on ScienceDirect®.

Regular Articles

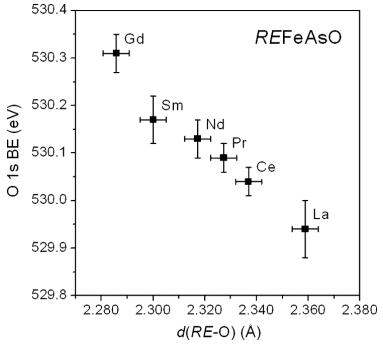

In the rare-earth oxyarsenides *RE*FeAsO, the oxygen 1*s* binding energy increases upon substitution with a smaller *RE* metal (from La to Gd).

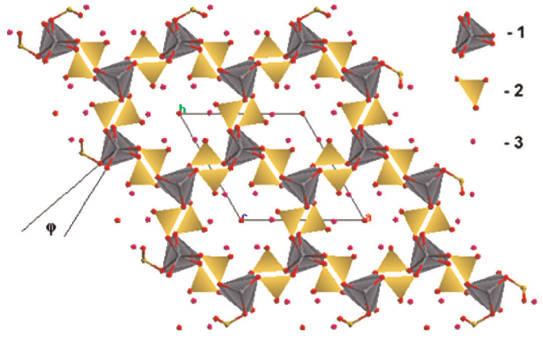

The fragment $Ca_4Bi_{4.3}(SiO_4)(HSiO_4)_5O_{0.95}$ structure along *c*-axis in polygonal mode.

Regular Articles—Continued

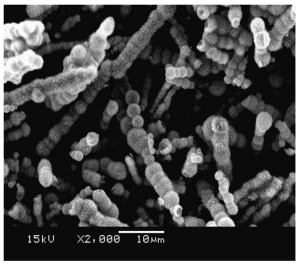

MnO_2 with a sea urchin-like ball chain shape is first synthesized in a high magnetic field via a simple hydrothermal route.

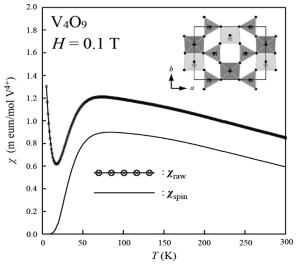

Temperature dependence of magnetic susceptibility (χ_{raw}) measured at 0.1 T for V_4O_9. The intrinsic d-spin susceptibility (χ_{spin}) of V_4O_9 after subtracting the Curie tail and the temperature-independent term is shown by the solid line. V_4O_9 is a spin-1/2 1D antiferromagnetic quantum spin system with a spin-gapped ground state. The structure of V_4O_9 is constructed from distorted VO_6 octahedra and VO_4 tetrahedra, similar to the structure of $(VO)_2P_2O_7$ with PO_4 tetrahedra instead of VO_4 tetrahedra.

Continued

Thermal decomposition behavior of the rare-earth ammonium sulfate $R_2(SO_4)_3 \cdot (NH_4)_2SO_4$
Tsukasa Nagai, Shinji Tamura and Nobuhito Imanaka
Page 1504

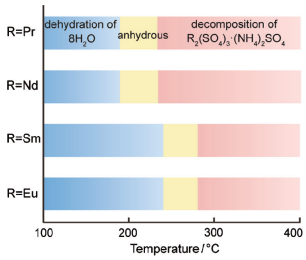

Stable temperature range of anhydrous rare-earth ammonium sulfate $R_2(SO_4)_3 \cdot (NH_4)_2SO_4$ was clarified by thermogravimetry/differential thermal analysis, infrared, Raman, and electrical conductivity measurements. Since the previous reports were based only on thermal analysis, the present work has more accurately determined the exact thermal stability of rare-earth ammonium sulfate solids.

Four divalent transition metal carboxyarylphosphonate compounds: Hydrothermal synthesis, structural chemistry and generalized 2D FTIR correlation spectroscopy studies
Ran Lei, Xiaochuan Chai, Hongxin Mei, Hanhui Zhang, Yiping Chen and Yanqiong Sun
Page 1510

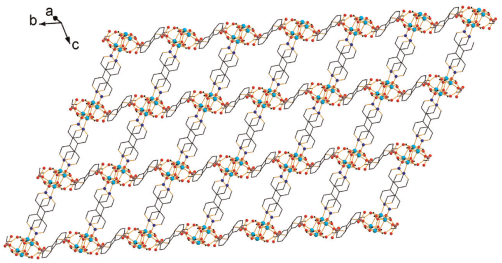

A series of divalent transition metal carboxyarylphosphonate compounds were synthesized under hydrothermal conditions. The figure displays 2D sheet structure with large windows in compound **2**.

First-principles study of the crystal and electronic structures of α-tetragonal boron
Wataru Hayami and Shigeki Otani
Page 1521

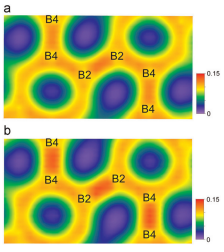

Calculated electron densities of B_{50} and $B_{50}+2B$ at site 4*c* (configuration B).

Crystal structure and physical properties of the quaternary manganese-bearing pavonite homologue $Mn_{1.34}Sn_{6.66}Bi_8Se_{20}$
Clarence Anglin, Nathan Takas, Juan Callejas and Pierre F.P. Poudeu
Page 1529

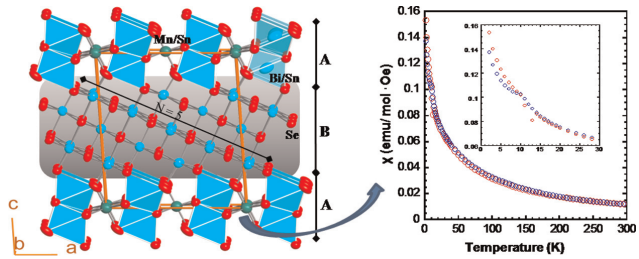

$Mn_{1.34}Sn_{6.66}Bi_8Se_{20}$, a narrow gap semiconducting and antiferromagnetic pavonite homologue obtained by partial substitution in octahedral position of Sn by magnetic Mn atoms.

Electronic structure of ZrCuSiAs and ZrCuSiP by X-ray photoelectron and absorption spectroscopy
Peter E.R. Blanchard, Ronald G. Cavell and Arthur Mar
Page 1536

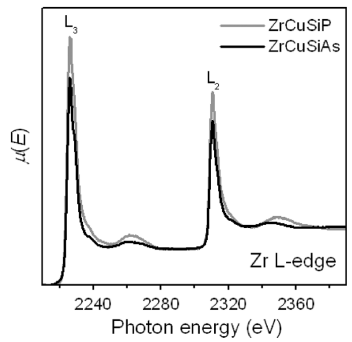

X-ray spectroscopy provides evidence for three-dimensional bonding character in ZrCuSiAs (and ZrCuSiP), the parent structure type for numerous superconducting oxypnictides.

Calcium-doped ceria/titanate tabular functional nanocomposite by layer-by-layer coating method
Xiang W. Liu, M.K. Devaraju, Shu Yin and Tsugio Sato
Page 1545

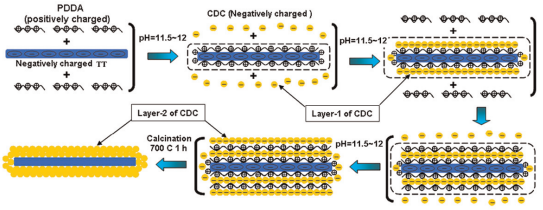

Through the control of surface charge of particles calcium-doped ceria/titanate composites with low oxidation catalytic activity, higher UV-shielding ability and excellent comfort was obtained by a facile layer-by-layer coating method.

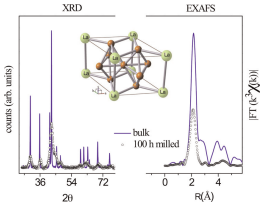

X-ray diffraction (XRD) pattern (left panel) and Fourier transforms of the Ni K-edge extended X-ray absorption fine structure (EXAFS) spectroscopy (right panel) of bulk $LaNi_5$ hydrogen storage material (structure model is given in the middle) together with the same after 100 h ball-milling. Milled samples show a remarkable reduction intensity and broadening of the XRD peaks. Substantial damping of the amplitude and a slight shrinkage of the profile are observed in the EXAFS spectrum. These results indicate that the ball-milling up to 100 h results in the production of nanoparticles characterized by slightly reduced unit-cell volume and substantial atomic disorder compared to the bulk LaNi5. High temperature annealing appears to help in partial recovery of atomic order in the ball-milled samples; however, long-time ball-milled samples retain the disorder even after the high temperature annealing. The results suggest that the large disorder and the reduced unit-cell volume might be causing a higher energy-barrier for the hydride-phase formation in the long-time ball-milled $LaNi_5$ powders.

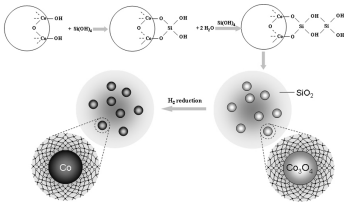

Co NPs are encapsulated by SiO_2 mediated by Si–O–Co bonds. This SiO_2 matrix stabilizes FCC-Co and improves the high-frequency performance of Co NPs.

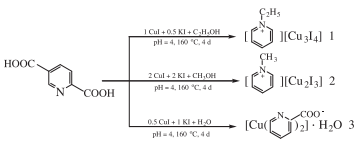

Three compounds were obtained via *in situ* metal–ligand hydro (solvo)thermal reactions of 2,5-$(cooh)_2$py with cui. Three types of *in situ* reactions occurred for 2,5-$(cooh)_2$py: decarboxylation *n*-ethylated in **1**, *n*-methylated in **2** and semi-decarboxylation in **3**.

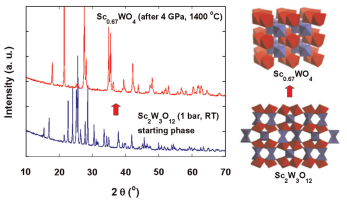

NTE material orthorhombic $Sc_2W_3O_{12}$ transforms into a new compound, $Sc_{0.67}WO_4$, when treated at 4 GPa and 1400 °C. $Sc_{0.67}WO_4$ has a defective wolframite structure, and is a paramagnet whose conductivity is that of a metal in the presence of weak localization and electron–electron interactions. Oxygen vacancies are suggested as a potential mechanism for generating the carriers in this material.

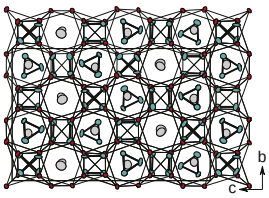

A metastable intermetallic compound with the composition $Zn_9Sb_6In_2$ has been identified in the ternary system Zn–Sb–In. Its structure relates to tetragonal $CuAl_2$ in that it contains 3^2434 nets (formed by the Sb atoms) that are stacked in antiposition orientation.

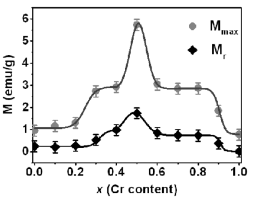

A series of perovskites $LaFe_{1-x}Cr_xO_3$ ($0 \le x \le 1$) were synthesized by mild hydrothermal method and characterized by their weak ferromagnetism due to the possible random distribution of Fe and Cr ions in B sites of the perovskites. The magnetic property of the perovskites is strongly dependent upon the compositions and a maximum magnetic moment is found for $LaFe_{1-x}Cr_xO_3$ at $x = 0.5$.

Continued

Metal diphosphonates with double-layer and pillared layered structures based on *N*-cyclohexylaminomethanediphosphonate

Yan-Hui Su, Deng-Ke Cao, Yan Duan, Yi-Zhi Li and Li-Min Zheng

Page 1588

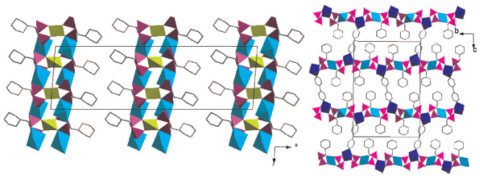

Based on *N*-cyclohexylaminomethanediphosphonate ($cmdp^{4-}$), compounds $Zn_3(cmdpH)_2(H_2O)_2$ (**1**) and $Co_3(cmdpH)_2(H_2O)_2$ (**2**) with a double-layer structure and compounds $Co_2(cmdpH_2)_2(4,4'\text{-bipy})_{0.5}(H_2O)$ (**3**) and $Mn_2(cmdpH_2)_2(4,4'\text{-bipy})_{0.5}(H_2O)$ (**4**) with a pillared layered structure are reported in this paper. Dominant antiferromagnetic interactions are found in compounds **2**–**4** and an interesting spin flop behavior is observed in **2**.

Single-crystal micro/nanostructures and thin films of lamellar molybdenum oxide by solid-state pyrolysis of organometallic derivatives of a cyclotriphosphazene

Carlos Díaz, Vladimir Lavayen and Colm O'Dwyer

Page 1595

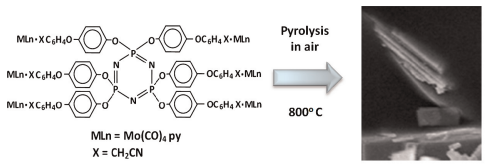

Lamellar MoO_3 micro- and nanocrystals are prepared by pyrolysis of the organometallics $N_3P_3[OC_6H_4CH_2CN \cdot Mo(CO)_5]_6$ (I) and $N_3P_3[OC_6H_4CH_2CN \cdot Mo(CO)_4\ py]_6$ (II), in air at 800 °C. The single-crystal products exhibit a high degree of turbostratic layering (see image). Deposition and subsequent pyrolysis of uniphasic MoO_3 from the precursors is also possible on suitable substrates and supports.

Crystal chemistry of thorium nitrates and chromates

Ginger E. Sigmon and Peter C. Burns

Page 1604

The structures and infrared spectra of four new Th nitrates and two Th chromates are reported. The coordination numbers of the Th cations range from nine to 12 in these compounds. Structural units consist of isolated clusters, chains, sheets and frameworks.

Exploring order–disorder structural transitions in the Li–Nb–N–O system: The new antifluorite oxynitride $Li_{11}NbN_4O_2$

J. Cabana, M. Casas-Cabanas, H.J. Santner, A. Fuertes and M.R. Palacín

Page 1609

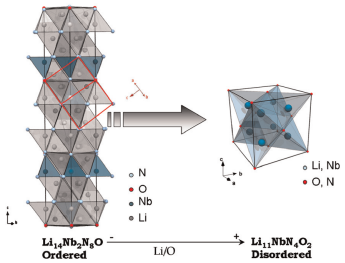

The Li–Nb–N–O system has been explored at low oxygen and high lithium contents and an order–disorder transition has been identified between ordered $Li_{16}NbN_8O$ and the new disordered $Li_{11}NbN_4O_2$ antifluorite-type oxynitrides.

Coordination polymer based on cyano: Synthesis, crystal structure, and fluorescence

Zhen-Lan Fang, Jian-Gang He, Qiang Ju, Xiao-Yuan Wu and Can-Zhong Lu

Page 1615

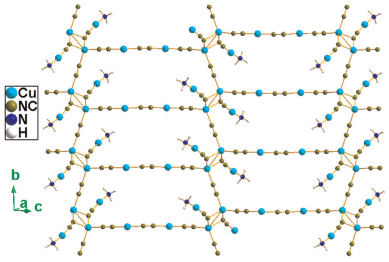

One novel 2-D polythreading framework $[Cu_3(CN)_3(NH_3)]$ (**1**) obtained through the self-assembling of CuCN under hydrothermal reaction shows bright yellow fluorescence at room temperature.

Synthesis and structural chemistry of $La_{18}Li_8Rh_4MO_{39}$ (M = Ti, Mn, Ru)

Peter D. Battle, Siân E. Dutton and Peter A. van Daesdonk

Page 1620

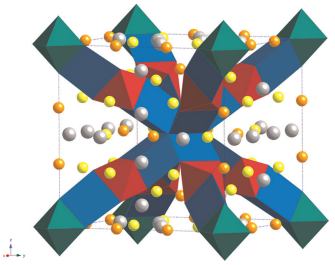

The substitution of Ti, Mn or Ru into $La_{18}Li_8Rh_5O_{39}$ results in the loss of the cation ordering seen in the parent compound.

Ionothermal synthesis and crystal structures of metal phosphate chains

David S. Wragg, Benjamin Le Ouay, Andrew M. Beale, Matthew G. O'Brien, Alexandra M.Z. Slawin, John E. Warren, Timothy J. Prior and Russell E. Morris

Page 1625

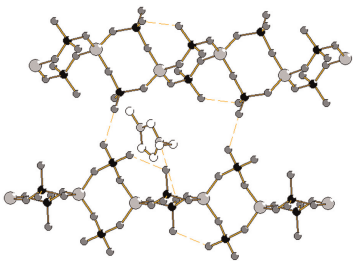

Chain structures prepared from ionic liquid solvents under a wide variety of synthesis conditions.

From 2-D CuO nanosheets to 3-D hollow nanospheres: interface-assisted synthesis, surface photovoltage properties and photocatalytic activity

Jun Zhu and Xuefeng Qian

Page 1632

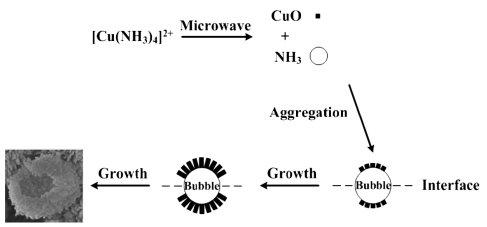

From 2-D CuO nanosheets to 3-D hollow nanospheres: interface-assisted synthesis, surface photovoltage properties and photocatalytic activity. Various CuO architectures with different morphologies and sizes, including hierarchical hollow nanostructures were prepared through a synergic bubble-template and interface-assisted approach.

$KBiMS_4$ (M = Si, Ge): Synthesis, structure, and electronic structure

Dajiang Mei, Zheshuai Lin, Lei Bai, Jiyong Yao, Peizhen Fu and Yicheng Wu

Page 1640

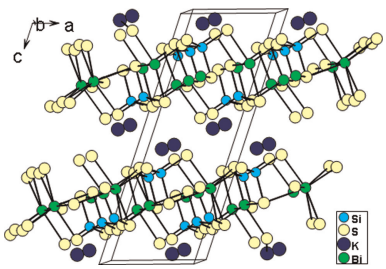

Two new bismuth sulfides $KBiSiS_4$ and $KBiGeS_4$ have been synthesized and characterized. The figure is the view down [0 1 0] of the crystal structure of $KBiSiS_4$.

Structural characterization and thermal properties of polyamide 6.6/Mg, Al/adipate-LDH nanocomposites obtained by solid state polymerization

M. Herrero, P. Benito, F.M. Labajos, V. Rives, Y.D. Zhu, G.C. Allen and J.M. Adams

Page 1645

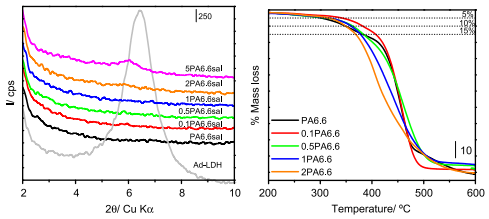

A new nanocomposite was obtained by compounding an adipate-modified layered double hydroxides (LDH) with adipic acid and hexamethylene diamine. These samples were polymerized in the solid phase under a nitrogen flow for 200 min at 190 °C. The nanodispersion of LDH in polyamide 6.6 may be qualitatively estimated from the analysis and PXRD patterns and FIB images. The decomposition temperature in the nanocomposite with 0.1 % LDH increases significantly compared to that for pristine PA6.6.

Structural and dielectric/ferroelectric properties of $(La_{1-x}Nd_x)_2Ti_2O_7$ synthesized by sol–gel route

Zhenmian Shao, Sébastien Saitzek, Pascal Roussel, Olivier Mentré, Felicia Prihor Gheorghiu, Liliana Mitoseriu and Rachel Desfeux

Page 1652

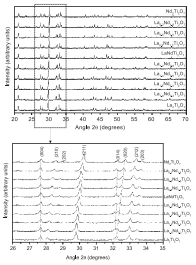

XRD patterns of $(La_{1-x}Nd_x)_2Ti_2O_7$ powders for various x values. The (hkl) peaks positions (with h and $k \neq 0$) change with x values while the (00l) peaks positions remain unaffected.

Moderate pressure synthesis of rare earth nickelate with metal–insulator transition using polymeric precursors

C. Napierala, C. Lepoittevin, M. Edely, L. Sauques, F. Giovanelli, P. Laffez and G. VanTedeloo

Page 1663

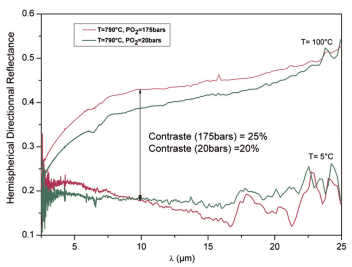

Thermochromic behavior of $Nd_{0.3}Sm_{0.7}NiO_3$ samples annealed under 20 and 175 bar at 278 and 373 K.

Continued

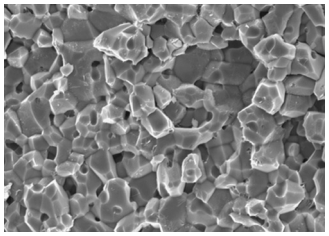

Representative microstructure of $Ca_2Fe_2O_5$ samples used for thermoelectrical measurements.

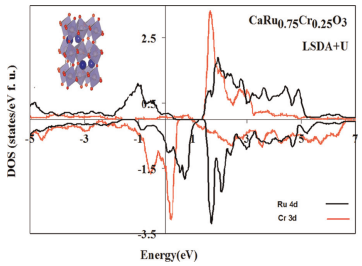

We have investigated the electronic structure of $Sr(Ca)Ru_{1-x}Cr_xO_3$ using different ab-initio calculation such as LSDA and LSDA + U approximation. The antiferromagnetic hybridization of Cr^{3+} with $Ru^{4+,5+}$ lattice increases the screening, which is consistent with the low magnetic moment of the Ru ions. The LSDA + U calculation for the more distorted Cr impurity doped Ca-based ruthenate compounds as compared to the Sr-based systems shows repulsion between electrons, which tends to keep the localized spins from overlapping.

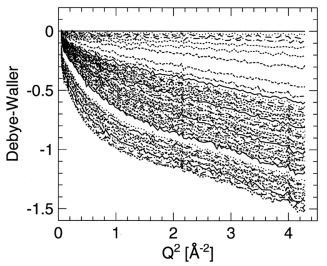

This paper concerns measurement of water dynamics associated within hydrophobic mesoporous organosilica material with phenyl functions as investigated using the quasielastic neutron scattering technique. By fitting the quasielastic neutron scattering results with Debye Waller factor, it show clearly the different behavior between water h inside and outside the hydrophobic pores.

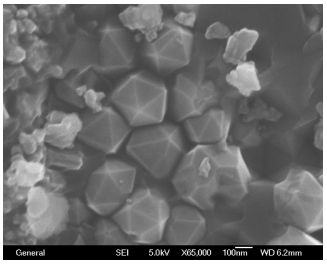

Icosahedral B_6O grains were prepared for mixtures of boron and ball milled boron oxide at 2 GPa and 1400 °C, a milder synthesis condition in comparison with previous works.

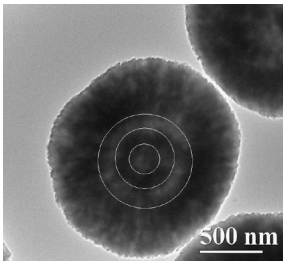

A variety of iron hydroxyl phosphate ($NH_4Fe_2(PO_4)_2OH \cdot 2H_2O$) nanostructures were synthesized by a simple one-step microwave-solvothermal ionic liquid method. Structural dependent photoluminescence was observed from the double-shelled hollow microspheres.

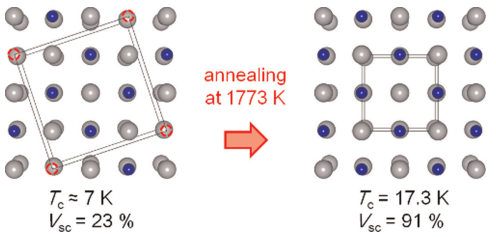

The $Nb_{0.89}Al_{0.11}$ oxynitrides exhibit a structural transformation in the course of high-temperature annealing, involving significantly enhanced superconductive characteristics.

Synthesis, photophysical and oxygen-sensing properties of a novel Eu^{3+} complex incorporated in mesoporous MCM-41
Qinghui Zuo, Bin Li, Liming Zhang, Yinghui Wang, Yanhong Liu, Jun Zhang, Ying Chen and Lifan Guo
Page 1715

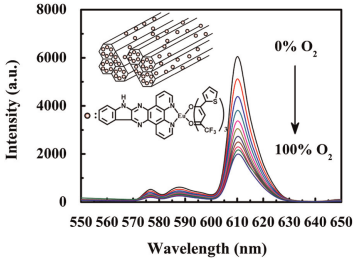

Novel optical oxygen-sensing composites are prepared by incorporating a novel Eu^{3+} complex $Eu(DPIQ)(TTA)_3$ into MCM-41. The emission intensity of $Eu(DPIQ)(TTA)_3$/MCM-41 composites exhibits a strong oxygen dependent characteristic and the composite with a loading level of 20 mg/g possesses better fluorescence quenching with increasing oxygen concentrations.

One-step synthesis of novel biacidic carbon via hydrothermal carbonization
Huiquan Xiao, Yingxue Guo, Xuezheng Liang and Chenze Qi
Page 1721

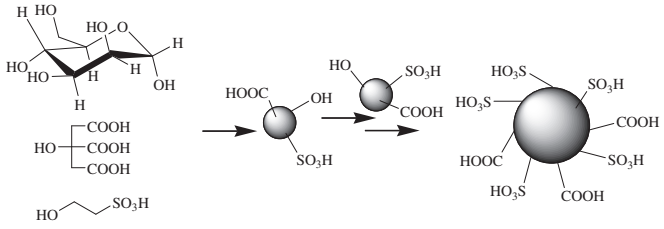

The novel biacidic carbon has been synthesized via one-step hydrothermal carbonization. Both the sulfonic and carbonyl acid groups were introduced to the carbon during the carbonization processes.

Structural, magnetic, and electrochemical studies on lithium insertion materials $LiNi_{1-x}Co_xO_2$ with $0 \le x \le 0.25$
Kazuhiko Mukai, Jun Sugiyama and Yoshifumi Aoki
Page 1726

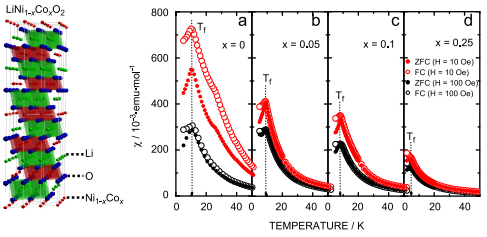

The inter-relationship between structural, magnetic, and electrochemical properties of the lithium insertion materials $LiNi_{1-x}Co_xO_2$ with $0x0.25$ were investigated by X-ray diffraction measurements, magnetic susceptibility measurements, and electrochemical charge and discharge test in non-aqueous lithium cell. The magnitude of spin-glass-like transition temperature T_f was found to decrease almost linearly with x, as well as the x dependences of effective magnetic moment, Weiss temperature, and lattice parameters.

Effects of gold catalysts and thermal evaporation method modifications on the growth process of $Zn_{1-x}Mg_xO$ nanowires
Ramin Yousefi and Muhamad Rasat Muhamad
Page 1733

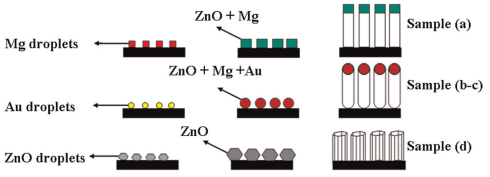

ZnMgO nanowires can be formed with and without gold catalyst by a modified thermal evaporation method.

Continued